8-1-2023

MIL-53(Fe) derived magnetic CuFe2O4/Fe2O3 composite for catalytic oxidation of sulfamethoxazole via peroxymonsulfate activation

Abdul H. Asif
Edith Cowan University

Nasir Rafique
Edith Cowan University

Rajan A. K. Hirani
Edith Cowan University

Lei Shi

Yantao Wang

See next page for additional authors

Authors

Abdul H. Asif, Nasir Rafique, Rajan A. K. Hirani, Lei Shi, Yantao Wang, Xiaoguang Duan, Yu Yin, and Hongqi
Sun

MIL-53(Fe) derived magnetic CuFe$_2$O$_4$/Fe$_2$O$_3$ composite for catalytic oxidation of sulfamethoxazole via peroxymonsulfate activation

Abdul Hannan Asif [a], Nasir Rafique [a], Rajan Arjan Kalyan Hirani [a], Lei Shi [b], Yantao Wang [c], Xiaoguang Duan [c], Yu Yin [d], Hongqi Sun [a,*]

[a] School of Science, Edith Cowan University, Joondalup 6027, Australia
[b] College of Materials Science and Engineering, Nanjing Forestry University, Nanjing 210037, China
[c] School of Chemical Engineering, The University of Adelaide, SA 5005, Australia
[d] School of Environmental and Chemical Engineering, Jiangsu University of Science and Technology, Zhenjiang 212003, China

ARTICLE INFO

ABSTRACT

Design of metal–organic framework (MOF) derived metal oxides is an effective approach for environmental remediation. The current study describes the fabrication of MIL-53-derived perforated CuFe$_2$O$_4$/Fe$_2$O$_3$ using a facile, one-step, post-thermal solid-state approach by varying Cu/Fe ratios. Herein, the release of CO$_2$ and H$_2$O during the thermal treatment facilitates the incorporation of Cu^{2+} onto the Fe$_2$O$_3$ structure, forming a perforated hollow CuFe$_2$O$_4$/Fe$_2$O$_3$ composite via an in-situ ion-exchange mechanism. The optimised catalyst CF-0.5 displays a high degradation efficiency for the removal of sulfamethoxazole (SMX) by heterogeneous activation of peroxymonsulfate (PMS), ascribing to the better textural, morphological, and elemental properties of the novel catalyst. Important reaction parameters such as pH, catalyst loading, PMS dosage, pollutant kind and concentration, and reaction temperature are further optimised to develop a cost-effective catalytic system. The magnetically recoverable catalyst outlines a high stability rate, and only a 9 % efficiency loss is observed even after the fourth cycle. Reactive oxygen species (ROS) are identified by electron paramagnetic resonance spectroscopy (EPR) and their roles are determined by performing quenching experiments. In the end, a detailed study of the mineralisation ability and reaction intermediates is performed and possible pathways for the degradation mechanism are proposed. This study not only introduces a facile approach for the fabrication of MOF-driven nanomaterials but provides insights into the removal of emerging contaminants such as SMX.

1. Introduction

Owing to their excessive utilisation, penetration and accumulation into the aquatic systems, pharmaceutical pollution is posing adverse effects on human and marine life and therefore being enlisted under "Emerging Contaminants (ECs)" [1,2]. Sulfamethoxazole (SMX), a sulfonamide antibiotic, is frequently used in both human and veterinaries medication against bacterial infections [3]. As a result of its effective control over bacterial diseases, the increased consumption of SMX has resulted in its accumulation and therefore continuously been detected in the range of $0.01 - 2$ g L^{-1} as reported by previous studies [3,4]. Though the reported values are not an immediate threat, its continuous discharge can increase the SMX concertation, inducing chronic diseases and genetic mutation. Additionally, prolonged exposure can enhance antibiotic resistance in bacteria [5]. Therefore, it's the need of the hour to exploit new routes/technologies to detoxify the aquatic environment from SMX pollution.

In comparison to the traditional Fenton or Fenton-like processes, sulfate radical-based AOPs (SR-AOPs) have emerged as an effective technology to counter and eliminate persistent pollutants [6]. In principle, hydroxyl radical-based AOPs (HR-AOPs) primarily generate hydroxyl radicals ($^\bullet$OH), whereas the latter enjoy the generation of additional sulfate radicals (SO$_4^{\bullet-}$) along with $^\bullet$OH, during the activation of peroxymonosulfate (PMS) or peroxydisulfate (PDS) [7–9]. Taking advantage of a longer half-life and higher redox potential (3.1 eV) of sulfate radicals, SR-AOPs can effectively degrade refractory contaminants, endocrine disruptors and personal care products (PCPs) [10]. Moreover, SO$_4^{\bullet-}$ can be generated in a wide pH range ($2 - 11$) and therefore has an extra advantage over $^\bullet$OH, which is most likely restricted to acidic conditions only [11]. Depending on nature of the

catalytic system, the generation of other reactive species such as superoxide ($O_2^{\bullet-}$) and sometimes singlet oxygen ($^1O_2$) are also well-reported during the activation of PMS [12]. Regardless of their low redox potential, these species can degrade organic contaminants to some extent but follow a different degradation mechanism/path [13,14].

Hematite (α-Fe$_2$O$_3$), an environment-friendly and the most abundant form of iron oxide, has been frequently employed for the catalytic activation of PMS/PS [15–17]. However, the heterogeneous catalytic system has its shortcomings e.g., i) poor regeneration of Fe^{2+}, ii) excess amount of Fe^{3+} on the catalyst surface and/or, iii) metal-ions leaching in case of a high catalyst dosage [18]. In the past decade, the fabrication of spinel ferrites (MFe$_2$O$_4$) had emerged as a promising solution to address the associated problems of α-Fe$_2$O$_3$ catalytic systems [19]. Here, the synergistic effect of the coupled transition metal oxide MFe$_2$O$_4$ (M = Co, Cu, Mn, Ni…) with Fe$_2$O$_3$ can further tune its physicochemical properties along with induced high magnetisation, resulting in the enhanced catalytic activity and better recycling ability [20,21]. In connection with the spinel family, CuFe$_2$O$_4$ is proven to be an efficient spinel catalytic material for the degradation of organic contaminants via PMS activation [22–24]. Apart from its efficiency in environmental remediation, its widespread application is limited by strong magnetisation, intermolecular interactions and poor electrical conductivity which can significantly affect its catalytic performance by reducing the exposed sites and poor electron mobility [25,26].

To overcome these challenges, metal–organic framework (MOF)-derived Fe$_2$O$_3$ can be one promising alternative for the fabrication of an efficient catalytic system [27]. Being a self-sacrificial template, MOF-driven catalysts enjoy the presence of carbon skeleton to some extent and can thus enhance the electronic conductivity of the resultant catalyst [28]. Additionally, the high porosity can further induce more active sites for the adsorption of organic contaminants onto the catalyst surface, resulting in the better degradation of organic contaminants [29,30]. Despite the extensive research available on the fabrication of spinel structure and MOF-driven Fe$_2$O$_3$, it is still a challenge to incorporate these two materials into one another to attain maximum catalytic efficiency.

Inspired by the above observation, a novel CuFe$_2$O$_4$/Fe$_2$O$_3$ (CF-x) perforated bipyramidal structure is fabricated by a simple one-step MOF-driven approach. The fabricated CF-x catalyst depicted better textural, morphological and elemental properties, as analysed by comprehensive physiochemical techniques. Afterwards, the as-prepared catalytic materials were employed for the degradation of SMX via PMS activation. Among all CF-x materials, the CF-0.5 catalyst exhibited high catalytic activity and was able to achieve 99.9 % removal efficiency for 20 mg L^{-1} SMX in just 45 min. Important reaction parameters such as pH, temperature, PMS dosage and catalyst loading were further optimised to achieve a cost-effective but efficient catalyst system. Above all, the catalyst was recovered/recycled by applying an external magnet and depicted high stability even after four cycles. Quenching experiments and electron paramagnetic resonance spectra (EPR) identified and confirmed the presence of both radical (SO$_4^{\bullet-}$, $^\bullet$OH, and O$_2^{\bullet-}$) and non-radical ($^1O_2$) species. In the end, the mineralisation ability of the proposed catalytic system was analysed through total organic carbon (TOC) analysis and possible degradation pathways were proposed. This work not only exploits a facile strategy for the fabrication of magnetically recoverable CuFe$_2$O$_4$/Fe$_2$O$_3$ catalyst but provides deep insights into the removal of emerging contaminants.

2. Materials and methods

2.1. Chemicals and reagents

All the chemicals and reagents with grade information are detailed in supplementary information as Text S1.

2.2. Fabrication of Cu-modified MOF and CuFe$_2$O$_4$/Fe$_2$O$_3$

MIL-53(Fe) was first prepared by a previously reported method and detailed in supplementary Text S2 [31]. For the synthesis of CuFe$_2$O$_4$/Fe$_2$O$_3$, copper acetate and Fe-MOF were first dispersed in 30 mL absolute ethanol by maintaining different weight ratios of Cu content to Fe-MOF (Cu/MOF = x), where x = 0.25, 0.5 and 0.75. The above mixture was ultrasonicated for 30 min and then placed in an oven at 80 °C to evaporate the ethanol. After that, the dried powder was placed in a ceramic crucible and calcined at 500 °C for 4 h in a muffle furnace to remove the impurity acetate groups. Pristine α-Fe$_2$O$_3$ was prepared by directly calcining Fe-MOF at 500 °C for 4 h. Whereas pure CuFe$_2$O$_4$ was fabricated by raising Cu/MOF ratio to 1.25 at similar conditions.

2.3. Characterisation

All the characterisation techniques with equipment specifications are detailed in supplementary Text S3.

2.4. Experimental procedure

The detailed experimental procedure and the analytical techniques are outlined in Text S4 and Text S5 in supplementary section.

2.5. Theoretical chemical calculations (DFT analyses)

The detailed visualization and chemical calculations were performed on VASP and are provided in supplementary information as Text S6.

3. Results and discussion

3.1. XRD, FT-IR, XPS, textural, and morphological analyses

Phase identification and sample purity were analysed by X-Ray diffraction (XRD) patterns. Fig. S1 depicts the XRD pattern of as-prepared MOF which is in close resemblance with MIL-53 (Fe), indicating the successful formation of MIL-53(Fe). After calcination, the obvious peaks of MIL-53 disappeared and new peaks of α-Fe$_2$O$_3$ emerged at position 2θ = 28.08, 38.6, 41.5, 47.8, 58.09, 63.6, and 68.1, and are well-aligned to JCPDS 33–0664, suggesting the complete conversion of MIL-53 to α-Fe$_2$O$_3$ during the calcination process (Fig. 1a). In comparison to the pure Fe$_2$O$_3$, the addition of Cu precursor has caused the appearance of some explicit peaks at position 2θ = 37.9, 41.5, 45.8, 54.7, 57.2, 63.01 and 68.8, indicating the successful interaction of Cu/Fe ions to form a spinal CuFe$_2$O$_4$ (JCPDS 34–0425) [32]. Furthermore, a significant lowering in the characteristic peaks of the pure α-Fe$_2$O$_3$ phase was also observed under the influence of Cu precursor, which further implies the formation of CuFe$_2$O$_4$/Fe$_2$O$_3$ structure by the ion-exchange method [33]. The successful fabrication of the CuFe$_2$O$_4$/Fe$_2$O$_3$ composite could be attributed to the in-situ reactions of surface-coated Cu^{2+} ions and Fe$_2$O$_3$ to form CuFe$_2$O$_4$ on the surface of α-Fe$_2$O$_3$. As the Cu/Fe ratio in the precursor solution increases, the peak intensities of Fe$_2$O$_3$ decrease but the respective characteristic peaks of CuFe$_2$O$_4$ increase. Upon further increase of Cu/Fe ratio, the participation of all Fe$_2$O$_3$ in the solid-state reaction was confirmed by the extinction of Fe$_2$O$_3$ peaks with the formation of CuO, whose diffraction peaks at 2θ = 41.5, and 45.8 are evident of a solid-state reaction between surface coated Cu^{2+} ions and Fe$_2$O$_3$.

Fourier-transform infrared (FT-IR) spectroscopy analyses were performed to evaluate the functional chemistry of as-prepared nanocomposites. At first, MIL-53(Fe) depicted the identical spectrum as that in the available literature (Fig. S2). One absorption band at 1596 cm^{-1}, and two sharp vibrational modes at 1505 and 1385 cm^{-1} are ascribed to the typical C = O, and C–O band stretching, respectively, indicating the successful coordination of organic linker into the MOF structure [34]. The respective peaks at 747 and 545 cm^{-1} are found to be aligned with
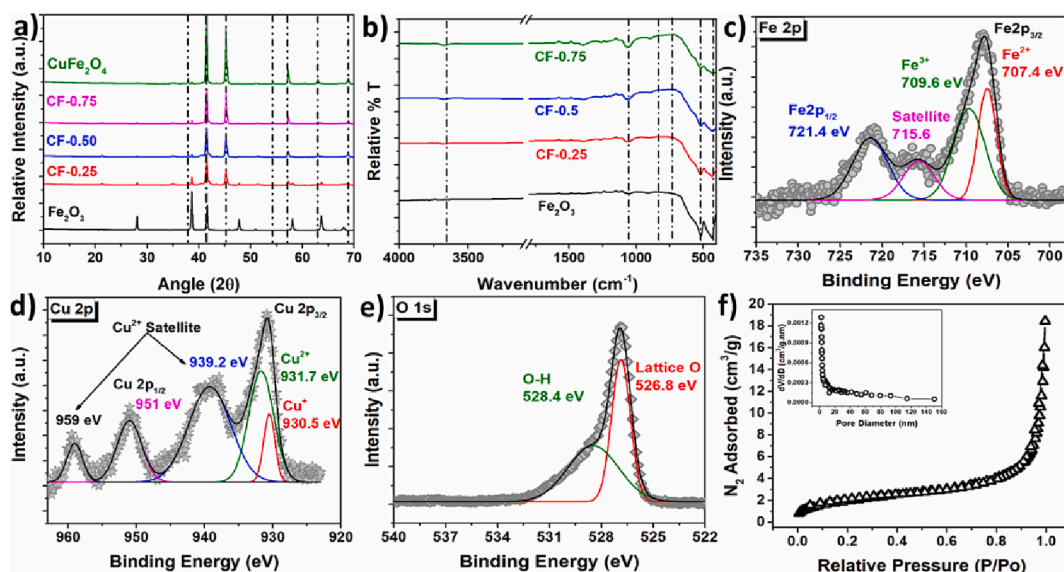
Fig. 1. a) XRD patterns of MOF-derived α-Fe$_2$O$_3$, and Cu-modified samples, b) FT-IR spectra of MOF-derived α-Fe$_2$O$_3$, and Cu-modified samples; High-resolution deconvoluted XPS spectra of c) Fe 2p, d) Cu 2p, and e) O 1 s of Cu-0.5 samples, and f) N$_2$ adsorption–desorption isotherm, (inset) pore size distribution of CF-0.5 sample.

the C–H band stretching of the benzene ring, and Fe–O band vibrations [35]. Furthermore, the wide band vibration at 3390 cm^{-1} is assigned to the typical O–H stretching, which could be due to the surface adsorbed water molecules. However, no band vibrations of the organic linker were observed in the fabricated α–Fe$_2$O$_3$, and CF-x nanocomposites, indicating the removal of 1,4-BDC at high temperatures (Fig. 1b). Furthermore, no band stretching of acetate precursor was observed in the CF-x structures, suggesting the high purity of the samples. Here, the characteristic bands at 434, and 516 cm^{-1} can be attributed to the typical metal–oxygen vibrational nodes (M−O; Cu–O, and Fe-O). Slight vibration at 896 cm^{-1} was identified in the CF-x spectra, evidencing the formation of a typical ferrite structure [36]. The presence of two slight bands stretching in the 1000 – 1500 cm^{-1} region can be due to the residual acetate impurities (COO$^-$), indicating the successful interaction of Cu/Fe with the precursor carboxylic impurities [37]. A weak vibration mode in the 3350–3400 cm^{-1} region indicates the removal of surface adsorbed water molecules during the high-temperature calcination process.

X-ray photoelectron spectroscopy (XPS) analyses were performed on CF-0.5 catalyst to have a deep insight into the chemical composition and oxidation states of respective elements. The catalyst composite was comprised of Cu, Fe and O elements. In high-resolution deconvoluted spectra of Fe 2p, two peaks positioned at 707.84 and 721. 6 eV were ascribed to the typical characteristic peaks of Fe 2p$_{3/2}$ and Fe 2p$_{1/2}$, respectively (Fig. 1c) [38]. Further deconvolution of Fe 2p$_{3/2}$ revealed the presence of Fe^{2+} and Fe^{3+} oxidation states at a binding energy of 707.4 and 709.6 eV, indicating the possible reduction of Fe^{3+} to Fe^{2+} during the high-temperature calcination process [39]. However, the appearance of a characteristic satellite peak of Fe^{3+} at 715.6 eV confirmed the obvious formation of α-Fe$_2$O$_3$ rather than Fe$_3$O$_4$ [40]. The high-resolution deconvoluted spectra of Cu 2p can be fitted with Cu 2p$_{3/2}$ at 930.9 eV, Cu 2p$_{1/2}$ at 951 eV, along with the two satellite peaks of Cu^{2+} at 939.2, and 959 eV (Fig. 1d). Further fitting of Cu 2p$_{3/2}$ resulted in two newly emerged peaks of Cu$^+$, and Cu^{2+} at 930.5, and 931.7 eV, respectively, indicating the presence of thermally reduced Cu species on the catalyst surface [41]. However, the phase dominance of CuO can be referred to the presence of two strong characteristic Cu^{2+} satellite peaks, which would lead to the formation of the CuFe$_2$O$_4$ composite [42]. The corresponding O 1 s spectrum was further deconvoluted into two distinct peaks of lattice oxygen and the surface adsorbed hydroxyl

groups (OH), centring at 526.8, and 528.4 eV, respectively (Fig. 1e) [43]. Here, the respective elemental XPS deconvoluted spectra of CF-0.5 catalyst are providing conclusive evidence of the successful formation of CuFe$_2$O$_4$/Fe$_2$O$_3$ nanocomposite.

Specific surface area (SSA), and porosity are well-known influential factors in catalytic processes. Therefore, the textural properties and porosity of as-fabricated structures were investigated through nitrogen adsorption–desorption isotherms, and are summarised in Table 1 (Fig. S3, & Fig. 1f). As expected, MIL-53(Fe) shows a high SSA of 868.75 m^2/g with high porosity. Upon calcination, the SSA of α-Fe$_2$O$_3$ was reduced to 2.84 m^2/g, ascribing to the removal of organic linker from the pristine structure. Moreover, the Cu-modified structures showed a gradual increase in the surface area w.r.t the induced Cu contents, suggesting the deposition and induction of Cu species to enhance the specific surface area. In addition, all the CF-x catalysts depicted pore abundancy predominantly in the range of 2 – 40 nm, suggesting the presence of micro-, and mesopores on the catalyst surface. However, the SSA of CF-0.75 catalyst was observed to decrease to 4.13 m^2/g, suggesting the possible blocking of active sites and pores due to agglomeration of CuO species onto the catalyst surface. The high specific surface area and improved textural properties of CF-0.5 are expected to enhance the catalytic oxidation of SMX because of its effective interaction (sorption) with the organic contaminant.

The morphology of as-fabricated microstructures was first examined by SEM. Pristine MIL-53(Fe) depicts a polygonal structure with a smooth surface and cornered edges, having an average length and width of 3.2 1.1 μm (Fig. 2 (a & b)). Upon calcination, the MOF structure ruptured drastically, ascribing to the escaping of carbon linker at high calcination temperatures. Moreover, several smaller particles of α-Fe$_2$O$_3$ seemed to be interconnected, leaving small pores in between each other, to retain the original bipyramidal structure (Fig. S 4 (a &b)). The pores between

Table 1
Textural properties of MOF and MOF-derived catalytic materials.

Catalytic Material	Specific Surface Area (m^2/g)	Average Pore Size (nm)
MIL-53(Fe)	868.75	22.25
Fe$_2$O$_3$	2.84	18.23
CF-0.25	3.72	20.18
CF-0.50	6.81	14.23
CF-0.75	4.13	15.76
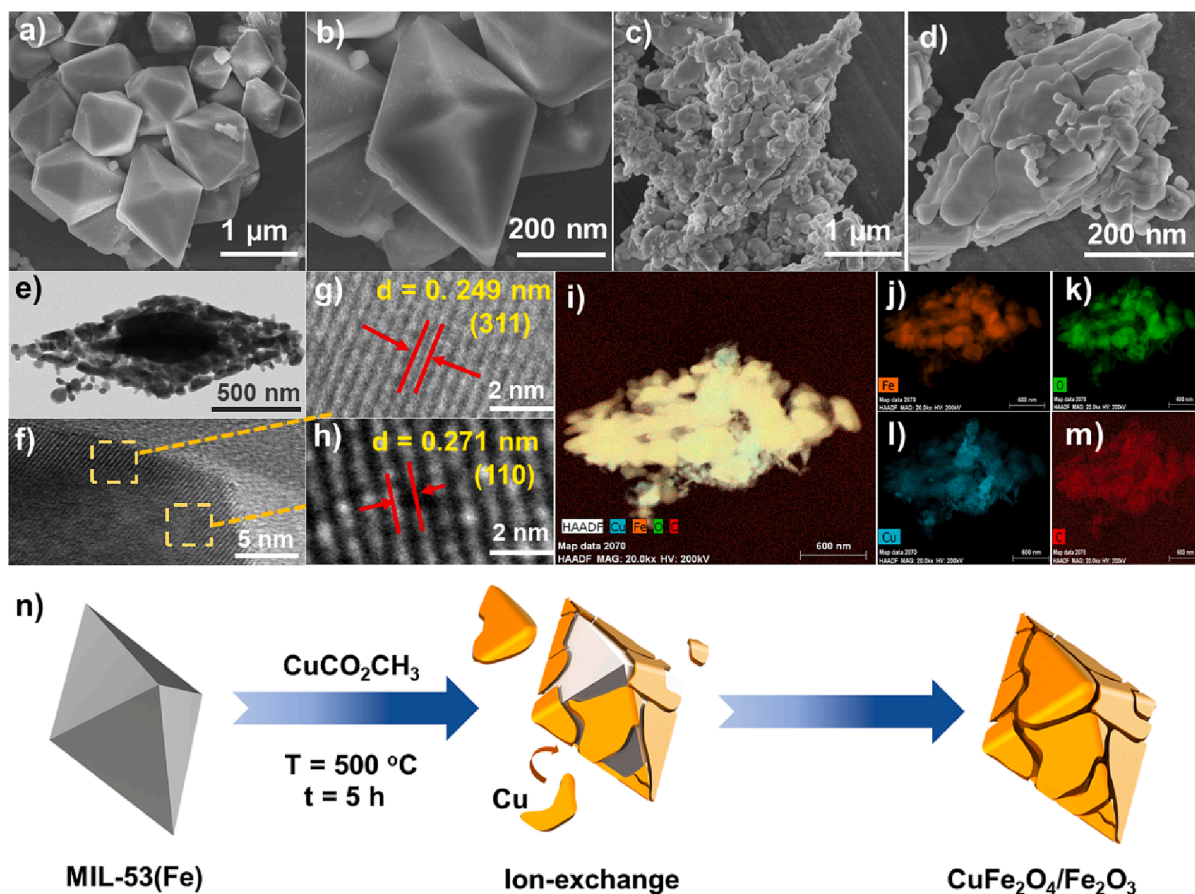
Fig. 2. SEM images of (a & b) MIL-53(Fe), and (c & d) CF-0.5 catalyst at different magnifications, (e) TEM image of CF-0.5, (f) HRTEM image of CF-0.5, (g - h) FFT pattern, and (i - m) EDX elemental mapping of the respective elements, and (n) schematic representation for the fabrication of CF-0.5 catalyst.

these small particles might be helpful for the effective diffusion of water molecules to show a better catalytic efficiency. However, the introduction of Cu precursor makes the surface coarser, as the aforesaid metal agglomerated on the surface of Fe_2O_3 (Fig. S4 (c & d)). It is evident from the SEM images that more the Cu-precursor is added, more agglomeration occurs on the surface of Cu-0.5 (Fig. 2 (c & d)). After exceeding a certain limit of Cu-addition (CF-0.50 catalyst), the excess Cu ions blocked the pristine active sites in the CF-0.75 catalyst, making it least effective for contaminant-catalyst interaction (Fig. S4 (e & f)). The results are also in-line with the BET surface area, where the SSA of CF-0.75 was observed to be smaller than the CF-0.5 catalyst.

The structural orientation and interfacial contact between Cu and Fe precursors at Cu-0.5 catalyst were further verified by TEM imaging. It is evident from the TEM image that the CF-0.5 composite is fabricated through the agglomeration of several small nanoparticles, ascribing to the release of H_2O and CO_2 during the solid-state calcination process (Fig. 2Fig. 2e). A high-resolution TEM (HRTEM) image further revealed the aggregation of irregular nanoparticles with lattice spacing (d-spacing) of 0.271 and 0.249 nm corresponding to the lattice planes of (110) of α-Fe_2O_3 and (311) of $CuFe_2O_4$, respectively (Fig. 2 (f - h)) . Furthermore, the EDX survey displays a near-uniform dispersion of all the elements onto the catalyst surface (Fig. 2 (i – m)). This intimate coordination between Fe_2O_3 and $CuFe_2O_4$ could be helpful to enhance the electrical conductivity of the newly fabricated $CuFe_2O_4/Fe_2O_3$ composite. Based on the aforesaid discussion, a schematic pattern for the fabrication of CF-0.5 catalyst is prepared and depicted in Fig. 2n.

The separation and transfer of electrons on catalyst surface was further analysed by performing electron impedance spectra (EIS). Herein, the semi-circle radius of Nyquist curve can be related to the charge transfer properties of the catalytic materials. To be more specific,

the smaller arc of the Nyquist curve can be attribute to better electrical conductivity and lesser resistance for electron migration [39]. Fig. 3 represents the smallest arc radius of CF-0.5 catalyst, representing minimal resistance for charge transfer, and the overall order of electrical conductivity could be represented as CF-0.5 > CF-0.75 > $CuFe_2O_4$ > CF-0.25 > Fe_2O_3. This lowest resistance of CF-0.5 can be concluded from the optimum ratio of (Cu/Fe), which is necessary to fabricate an efficient bimetallic catalyst.
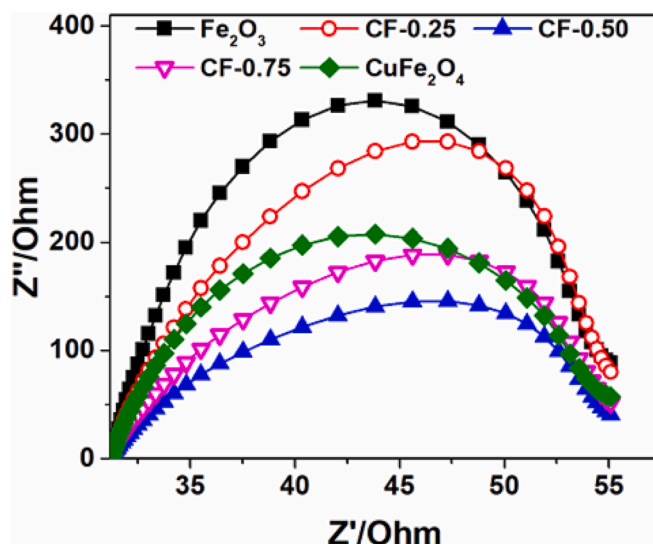
Fig. 3. Electron impedance spectra of as-fabricated catalysts.
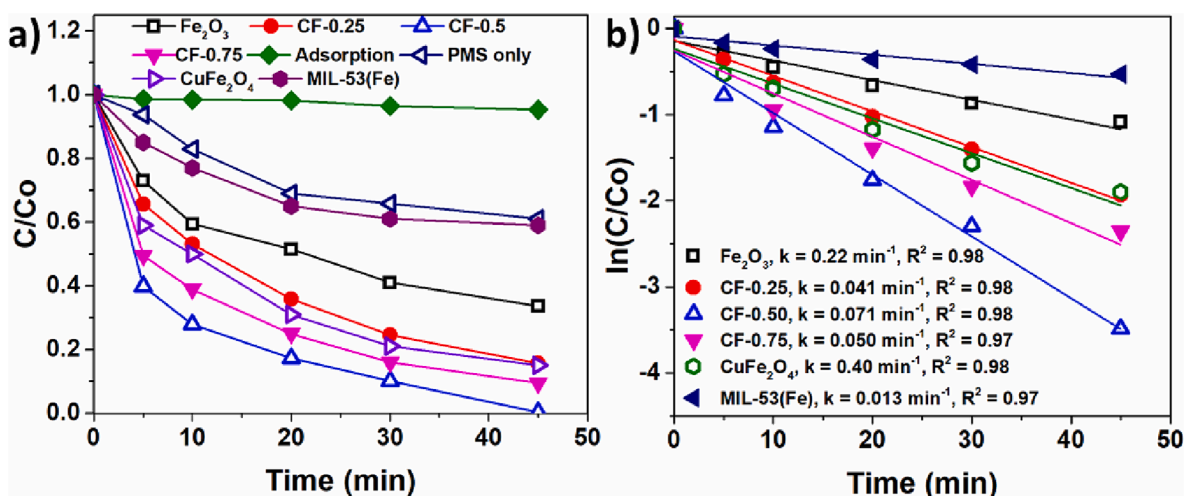
Fig. 4. (a) Catalytic oxidation of SMX under different catalytic systems, and (b) respective pseudo-first-order kinetics modelling; Reaction Condition: $[Catalyst]_0 =$ 0.2 g L^{-1}, $[SMX]_0 = 20$ mg L^{-1}, $[PMS]_0 = 6$ mM, and T = 25 °C.

3.2. Catalytic oxidation of SMX

The catalytic potential of as-prepared catalysts was evaluated in the removal of SMX via PMS activation (Fig. 4a). At first, 38 % SMX removal was recorded by PMS alone. This can be ascribed to the self-oxidation of PMS which results in the generation of singlet oxygen ($^1O_2$). Some recent studies have also reported the degradation of sulfonamides and other pharmaceutical molecules through a non-radical path during self-oxidation of PMS [44,45]. Moreover, the MIL-53/PMS catalytic system exhibited its limited effectiveness, as it only managed to remove $\sim$ 40 % SMX. However, the introduction of as-prepared catalysts, SMX degradation efficiency is progressively enhanced. Almost 67, 68, 85 and 99.7 % SMX degradation was observed by α-Fe$_2$O$_3$, CuFe$_2$O$_4$, CF-0.25, and CF-0.50 and PMS systems, respectively, and their respective reaction rate constants were recorded as 0.022, 0.040, 0.041 and 0.071 min^{-1} (Fig. 4b). This increase in reaction rate and degradation efficiency can be ascribed to better textural and morphological properties of Cu-modified Fe$_2$O$_3$ structure, which will ultimately provide more active sites with lesser charge migration resistance (Fig. 3). However, with a further increase in Cu contents, the catalytic performance of CF-0.75 for the degradation of SMX decreases to 90 % and its reaction rate also declined to 0.050 min^{-1}. The presence of excessive Cu contents will create a disordered interface with poor textural properties, resulting in the hampering of charge transfer properties on the catalyst surface (Fig. 3). The results suggest that the corresponding ratio of Cu/MOF has a considerable impact on the degradation efficiency of CF-x composites. Owing to the best performance of CF-0.5 catalyst, an adsorption experiment was performed under similar conditions, and only 5 % SMX removal was recorded by physical means.

3.3. Influence of key reaction parameters

To analyse the influence of key reaction parameters, the effect of PMS loading was first studied and examined by varying the initial PMS loading from 1.5 to 9 mM (Fig. 5a). A direct relationship was observed between PMS loading and the catalytic efficiency, as the respective degradation efficiencies were recorded as 73, 81, and 99.9 % for 1.5, 3 and 6 mM in just 45 min. The increased reaction rate can be due to more collisions between catalyst and oxidant to produce more active species, resulting in enhanced degradation efficiency (Fig. 5b). However, a mild improvement in degradation efficiency of SMX was observed when initial PMS dosage was further increased from 9 to 11 mM, as the reaction rate constant was slightly increased from 0.26 min^{-1} to 0.28 min^{-1}, respectively. Here the excess presence of PMS could hinder the

degradation efficiency by providing radial scavenging effect (Eq. (1). At the same time, self-quenching of SO$_4^{\bullet-}$ species could also play a decisive role in the degradation kinetics (Eq. (2) [46].

$$HSO_5^- + SO_4^{\bullet-} \rightarrow SO_5^{\bullet-} \tag{1}$$

$$SO_4^{\bullet-} + SO_4^{\bullet-} \rightarrow S_2O_8^{2-} \tag{2}$$

Fig. 5c depicts the effect of catalyst dosage on SMX degradation the respective reaction rate constants are illustrated in Fig. 5d. From the two figures, it is evident that the increased catalyst loading significantly enhanced the degradation efficiency. Nearly 20, 16, and 99.9 % SMX was successfully removed in 45 min, when 0.05, 0.1, and 0.2 g L^{-1} of catalyst were added to the reaction system. Their respective reaction rate constants were calculated as 0.036, 0.039, and 0.071 min^{-1} (Fig. 5d). An abrupt increase in the reaction rate from 0.071 to 0.28 min^{-1} was observed upon further increasing the catalyst dosage to 0.4 g L^{-1}. This increase in the degradation rate could be attributed to the availability of more active sites for the reaction with oxidant, accelerating the PMS activation efficiency (Fig. S5). Consequently, more reactive species would be generated to mineralise the target pollutant [47].

pH is a key factor for AOPs as most pharmaceutical and other pollutants have different pH and therefore may affect degradation efficiency. To evaluate this, the pH of the solution was adjusted by either 0.1 M HCl or 0.1 M NaOH (Fig. 5e). In a strong acidic pH condition (pH = 3), PMS activation slightly decreased to 13 % and the reaction rate constant was declined to 0.042 min^{-1} (Fig. 5f). This negative effect of lower pH might be because PMS is relatively stable under acidic conditions due to the presence of H$^+$ and its stabilisation effect on the leading specie of PMS, i.e., HSO$_5^-$. Furthermore, the possible bonding of H$^+$ and O–O group of HSO$_5^-$ may also provide additional hindrance for the catalyst-oxidant interactions [48]. In addition to this, dissolution of metal ions could also be another influential factor as a relatively higher leaching of metal ions was recorded at strong acidic conditions (pH = 3.01) (Fig. S6a). Upon increasing the initial pH value to the basic condition (pH = 9), a slight decline in the catalytic efficiency was observed and the reaction rate constant was dropped to 0.049 min^{-1}, possibly due to the negative effect of OH$^-$ ions. The excess amount of OH$^-$ ions will act as a scavenger for the SO$_4^{\bullet-}$, leaving behind the less reactive $^\bullet$OH radicals [49]. Furthermore, free metal ions (Fe and Cu) could also from hydroxides at higher pH values, inhibiting the overall degradation kinetics. Apparently, a drop in metal ions leaching was also recorded, recommending the stability of metallic oxide microstructure at higher pH values (Fig. S 6a). Another reason for the efficiency loss would be the adaption of non-radical ($^1O_2$) pathways, as PMS can be self-oxidised at
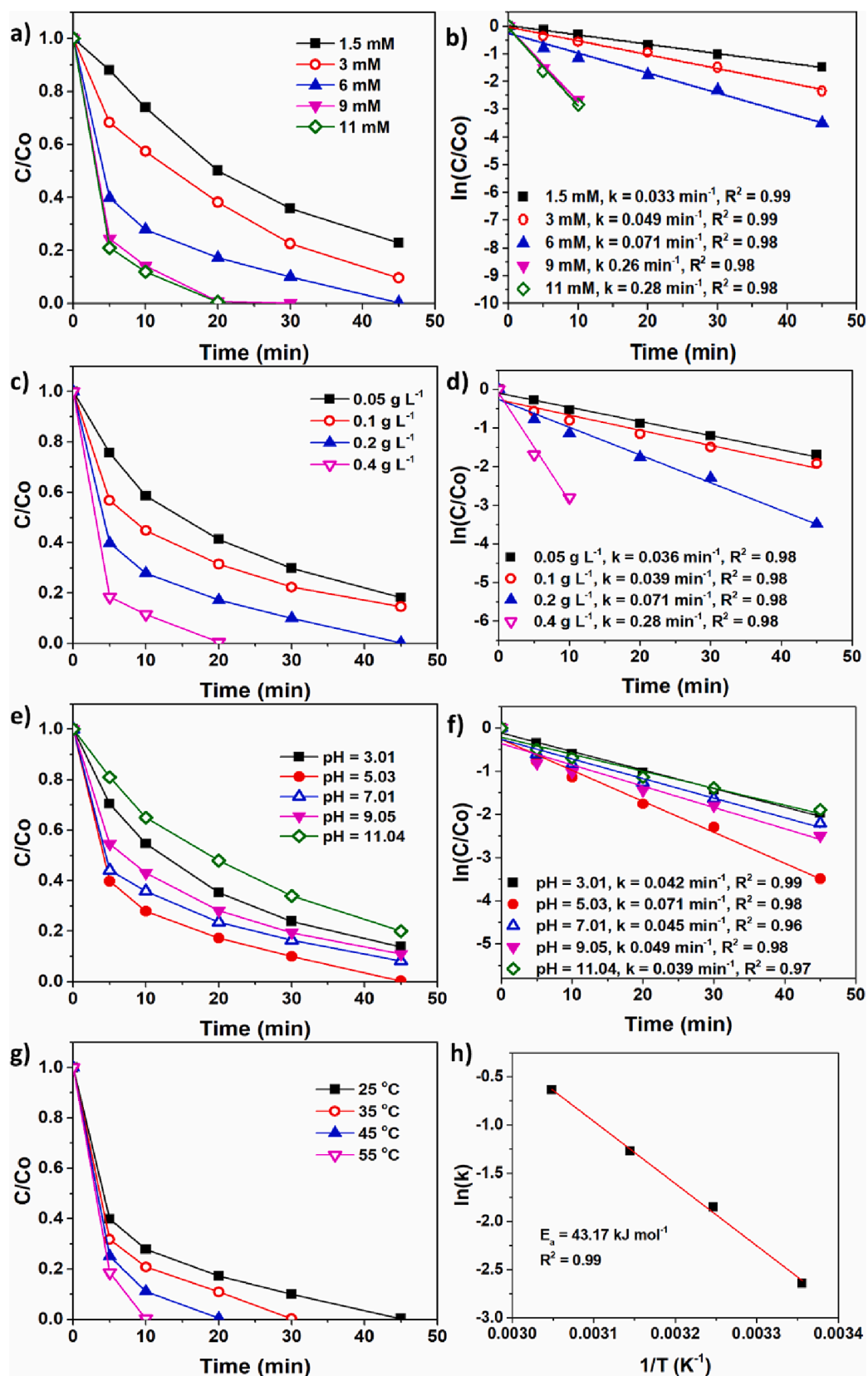
Fig. 5. Influence of reaction parameters (a) initial PMS concentration, (c) initial catalyst dosage, (e) initial pH, and (g) reaction temperature, (b, d, and f) the respective pseudo-first-order reaction kinetics, and (h) activation energy (Ea).

higher pH values, which would again minimise the generation of reactive radicals [50]. Moreover, the observed decline in degradation efficiency in harsh conditions (pH = 3 and11) can be attributed to the amphoteric nature of SMX, which exhibits two distinct pKa values (1.5 and 5.6) [51]. To be more specific, the associated amine (–NH$_2$) and amide (–NH-) groups are responsible for protonation and deprotonation at different pH. To better understand this, zeta potential of SMX/ CuFe$_2$O$_4$/FeO$_3$ catalytic system was investigated (Fig. S 6b). The increase of negative charge in extreme conditions pH (3 and 11) can induce mor electrostatic repulsion, resulting in the lower removal of SMX is observed. Slightly acidic and neutral solutions were found to be the best working conditions for the catalytic system. Contrarily, the material can still perform under a wide pH range (3 – 11), making it a potential working material for real-time applications.

The influence of reaction temperature was further evaluated by varying the reaction temperature in the range of 25 – 55 °C and depicted in Fig. 5g. A direct relationship between reaction temperature and reaction kinetics was recorded as the increase in reaction temperature significantly enhanced the reaction rate constants. Nearly, 100 % SMX degradation was achieved in 30, 20, and 10 min at the reaction temperatures of 35, 45, and 55 °C. Moreover, Arrhenius law was applied to calculate the activation energy of the CF-0.5 catalyst (Fig. 5h). The lower value of E$_a$ (43.17 kJ mol^{-1}) strongly recommends the application of the catalytic system for the removal of highly persistent chemicals such as SMX.

Effect of initial concentration on degradation efficiency was examined by varying the SMX concentration to 5, 10 and 50 mg L^{-1} (Fig. 6a). During the experiments, the initial dosages of both catalyst and PMS were kept consistent, ensuring a consistent number of generated reactive species. Consequently, a high initial SMX concentration (40 mg L^{-1}) will require an increased amount of both catalyst and PMS for achieving optimal degradation efficiency. In contrast, lower SMX concentrations of 5 and 10 mg L^{-1} were completely degraded in just 10 and 30 min, respectively. This notable degradation performance can be attributed to the exceptional application of the proposed CF-0.5/PMS catalytic system across a wide range of matrices.

The versatility of CF-0.5 catalyst was further demonstrated by employing the same catalytic system to target other pollutants, including phenol and other emerging contaminants such as p-hydroxy benzoic acid (p-HBA) and sulfachloropyridazine (SCP). Fig. 6b reveals the complete removal of these toxic pollutants within the specified time, illustrating the substantial efficacy of the CF-0.5/PMS catalytic system. This comprehensive degradation performance reinforces the versatile characteristics of the CF-0.5/PMS catalytic system, thus highlighting its potential suitability within a wide range of environmental contexts.
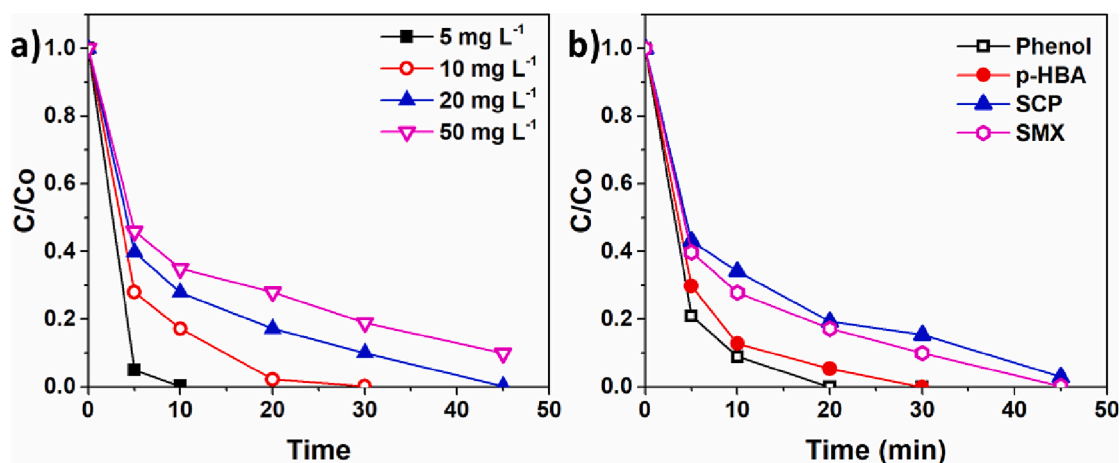
3.4. Catalyst stability and reusability

Catalyst stability and reusability are important as cost is a key factor in large-scale operations. To counter this factor, the catalyst was recovered with a magnet, thoroughly washed with ultrapure water, and kept at 60 °C for drying. The catalyst was used for three consecutive runs after the first use, and only 14 % efficiency loss along with a slight decline in the reaction rate constant was observed after 4th use (Fig. 7 (a & b)), ascribing to the residual occupation of active sites. Metal-ions leaching by Cu-0.5/PMS system was further monitored by using MP-AES (Fig. S 7a). In comparison to the respective iron ions leaching of 0.97 and 1.28 mg/L in Fe$_2$O$_3$/PMS and MIL-53(Fe)/PMS, only 0.3 mg/L of iron ions along with 0.21 mg/L of copper ions were determined in the leached solution of CF-0.5/PMS catalytic system. Apparently, Cu-modification on the Fe$_2$O$_3$ surface significantly depressed metal ions leaching during the catalytic process, suggesting the high stability of the CF-0.5 catalyst. Moreover, a heterogeneity test was performed by adding the leached amount along with PMS in the SMX solution (Fig. S 7b). And the SMX degradation efficiency was observed to be less than 40 % under the leached catalytic system in 45 min. The results are in-line with the PMS-only catalytic system, where a similar degradation efficiency was recorded earlier (Fig. 4a). These results conclusively suggest the successful activation of PMS by surface-bonded metallic species rather than the leached ions.

3.5. Mechanistic investigation and identification of reactive oxygen species

To have a more detailed insight into the role of surface-bonded elements, and the possible change in their chemical composition, XPS spectral analyses were performed on the fresh and used CF-0.5 catalyst. Apparently, all the peaks of respective elements (Cu, Fe, and O) were present in the survey scan of fresh and used catalysts, indicating their high chemical stability (Fig. 8a). In the high-resolution deconvoluted spectrum of Fe 2p fresh catalyst, the relative intensities of Fe^{+2}, and Fe^{3+} species at binding energies of 707.4, and 709.6 eV were recorded as 42.3 %, and 57.7 %, respectively (Fig. 8b). After the reaction, not only did the peak positions of the respective components slight shift to 707.5, and 709.8 eV, but their respective relative intensities were also changed to 37.7 %, and 62.3 %. This interconversion of the oxidation states depicts the partial contribution of Fe^{2+} species in the catalytic mechanism [52].

However, a dramatic change in the relative intensities of Cu species was observed after the reaction. In comparison to the fresh catalyst, the respective peaks of Cu^{2+}, and Cu$^+$ were shifted from 931.7 and 930.5 eV to 939.7 and 932.8 eV, respectively, in the used catalyst (Fig. 8c).

Fig. 6. (a) Effect of initial SMX concentration and (b) Catalytic oxidation of other pollutants. Reaction Condition: [Catalyst]$_0$ = 0.2 g L^{-1}, [SMX]$_0$ = [p-HBA]$_0$ = [SCP]$_0$ = [Phenol]$_0$ = 20 mg L^{-1}, [PMS]$_0$ = 6 mM, and T = 25 °C (In Fig. 6a SMX concentration was varied while keeping all other parameters constant).
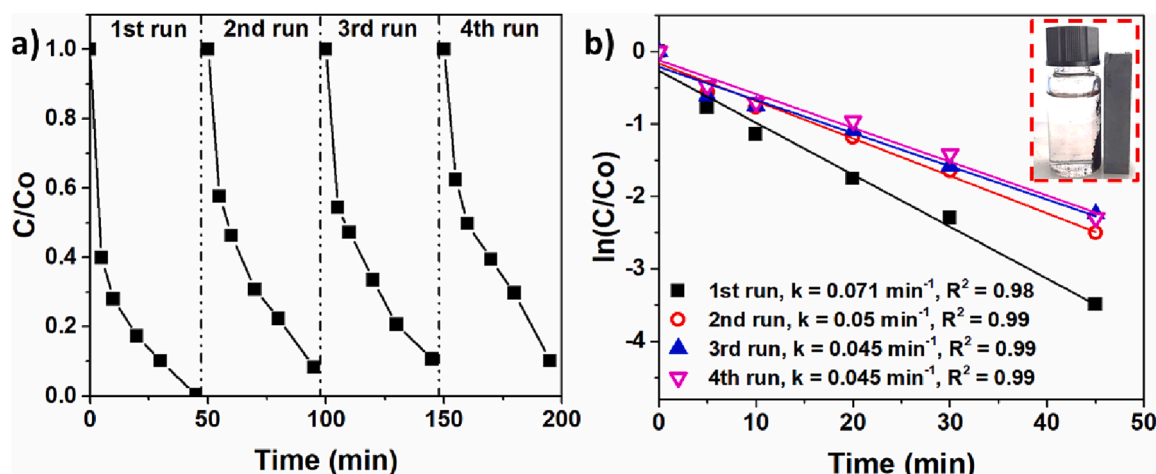
Fig. 7. (a) Stability test for CF-0.5, (b) the respective reaction rate constants, (inset) magnetic recovery. Reaction Condition: $[Catalyst]_0 = 0.2$ g L^{-1}, $[SMX]_0 = 20$ mg L^{-1}, $[PMS]_0 = 6$ mM, and T = 25 °C.
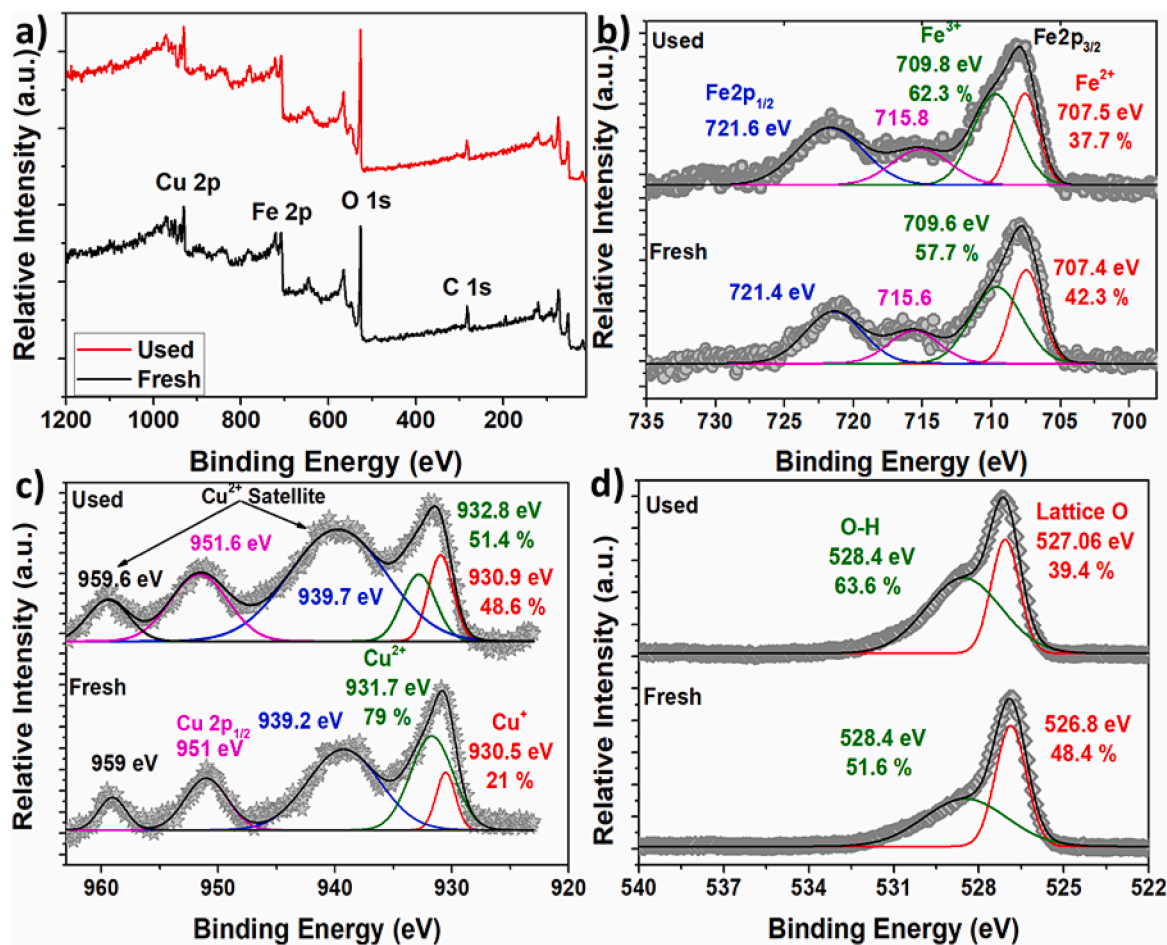
Fig. 8. Comparison of XPS spectra of fresh, and used catalyst (a) survey scan, (b) Fe 2p, (c) Cu 2p, and (d) O 1 s.

Moreover, their respective relative intensities were also changed from 79 % to 51.4 % for Cu^{2+}, and from 21 % to 48.6 %. The substantial change in the Cu oxidation states provides irrefutable evidence for the active participation of Cu^{2+} species in the catalytic oxidation reaction. The O 1 s spectra for fresh and used catalysts were further deconvoluted to analyse the role of oxygen species (Fig. 8d). After the reaction, a moderate change in the elemental states of oxygen was monitored, as the respective relative peak intensities were changed from 48.4 % to 39.4 %

for lattice O, and from 51.6 % to 63.6 % for surface adsorbed oxygen (O–H), indicating the hydroxylation of $CuFe_2O_4$ surface during the degradation reaction. The hydroxylation of the catalyst could be beneficial for the oxidation reaction, as the O–H sites can be served as the active sites for the effective generation of reactive oxygen species, which will ultimately boost the degradation reaction [53].

It is well reported that reactive oxygen species (ROS) such as $SO_4^{\bullet-}$, $^\bullet OH$, $O_2^{\bullet-}$, and $^1O_2$ are generated, and are held accountable for the

degradation of organic pollutants via PMS activation [12]. Therefore, identification of these ROS was first done by using DMPO and TEMP as spin trapping agents during electron paramagnetic resonance (EPR) analysis (Fig. 9 (a & b)). The addition of PMS without any catalyst results in the generation of a typical 1:2:2:1 spectrum for DMPO-SO$_4^{\bullet-}$ and DMPO-$^{\bullet}$OH adducts even after 20 min reaction, indicating the generation of SO$_4^{\bullet-}$ and $^{\bullet}$OH radicals. Interestingly, a distinguishable 1:1:1 triplet spectral signal for TEMP-^{1}O$_2$ adduct was also acquired, when TEMP was employed as a spin trapping agent. These results are reasonably justifying the degradation of SMX via self-oxidation of PMS (Fig. 4a). Moreover, the addition of the catalyst and PMS into the system would intensify the peak intensities of all the adducts, suggesting the enhanced generation of ROS by the CF-0.5 catalytic system. Additionally, the signal intensities of these adducts were following the order as DMPO-^{1}O$_2$ > DMPO-$^{\bullet}$OH > DMPO-SO$_4^{\bullet-}$ suggesting the generation of ^{1}O$_2$ during the PMS activation. The EPR results provide a direct evidence for the generation of radical (SO$_4^{\bullet-}$ and $^{\bullet}$OH) and no-radical (^{1}O$_2$) species in the CF-0.5/PMS catalytic system.

The presence and participation of these ROS were further evidenced by performing quenching experiments. Methanol (MeOH) can quench both SO$_4^{\bullet-}$, $^{\bullet}$OH radicals, whereas *tert*-butanol (tBA) can be used as a scavenger for $^{\bullet}$OH radicals [52]. At first, the added concentration of MeOH in the SMX solution was varied in the range of 10 – 50 mM, and a significant decrease in the degradation efficiency (82 % – 47 %) was observed (Fig. 9c). However, the degradation efficiency was dramatically dropped to below 10 %, when the added concentration of MeOH reached 100 mM. Moreover, the respective reaction rate constants were also recorded as 0.037, 0.0014, and 0.0008 min^{-1} against the MeOH concertation of 10, 50, and 100 mM (Fig. S 8a). Such a drastic effect of MeOH on SMX degradation efficiency strongly evidences the role of free radicals in the degradation mechanism. It was further observed that the effect of tBA, as $^{\bullet}$OH inhibitor, on the degradation of SMX, was not as adverse as of MeOH (Fig. (9d & S 8b)). As the SMX degradation efficiencies were dropped to 89, 73, and 62 %, when 10, 50, and 100 mM of tBA was added to the reaction solution, respectively, suggesting the leading role of SO$_4^{\bullet-}$ as a free radical species in the degradation of SMX. However, a minimal effect of oxygen anions (O$_2^{\bullet-}$) was observed, as the SMX degradation efficiency was dropped to 96, 83, and 78 %, reactively,
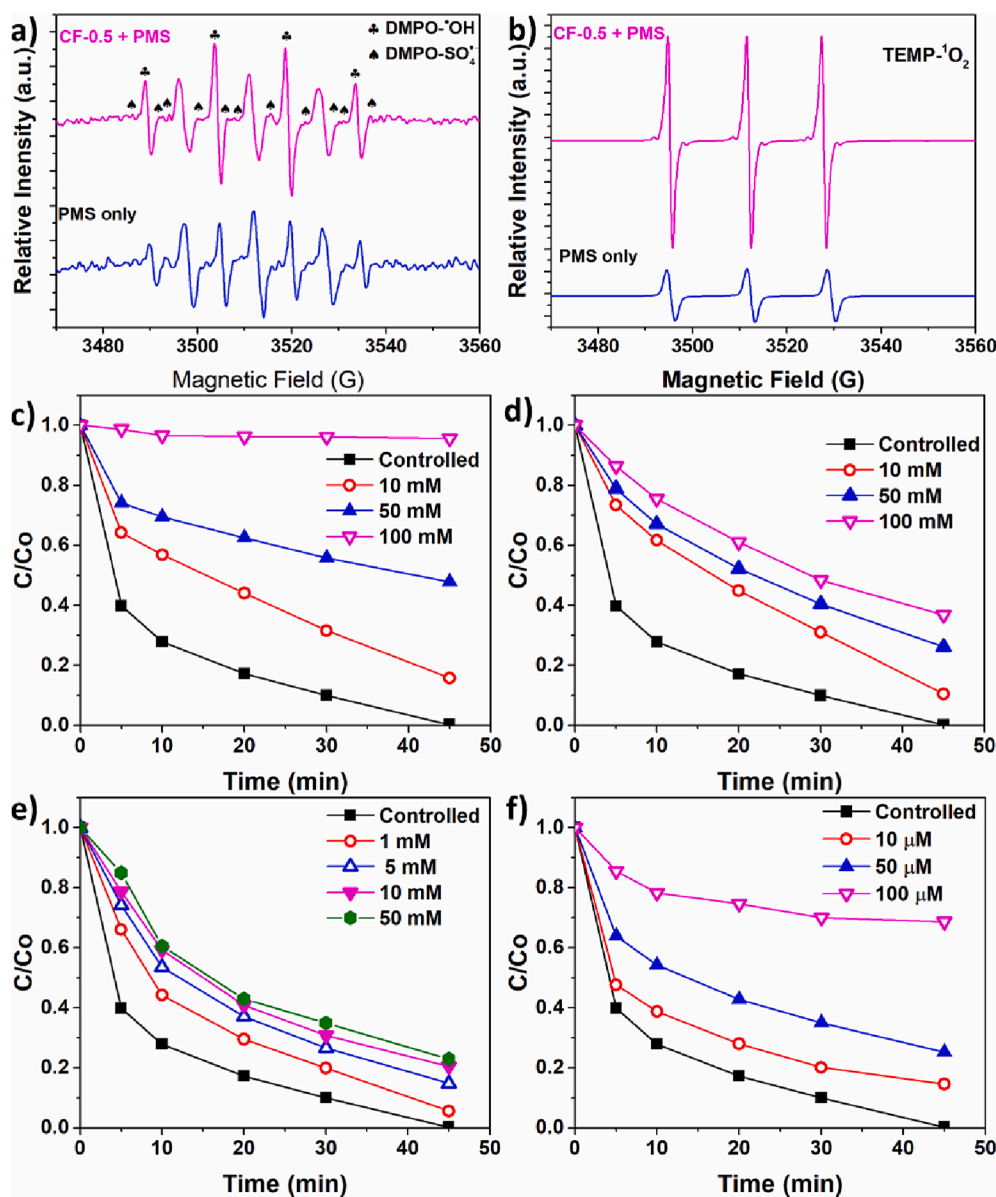
Fig. 9. EPR spectra for the identification of (a) SO$_4^{\bullet-}$, $^{\bullet}$OH and (b) ^{1}O$_2$, and quenching tests by using (c) methanol, (d) *tert*-butanol, (e) p-benzoquinone and (d) NaN$_3$. Reaction Condition: [Catalyst]$_0$ = 0.2 g L^{-1}, [SMX]$_0$ = 20 mg L^{-1}, [PMS]$_0$ = 6 mM, and T = 25 °C.

under the influence of 1, 5, and 10 mM of p-BQ (Fig. 9e & S 8c)). As singlet oxygen ($^1O_2$) was proven to be generated in the PMS-assisted oxidation systems by EPR analysis. Therefore, NaN_3 was added to analyse the possible effect of $^1O_2$ on the degradation of SMX (Fig. 9f). Interestingly, SMX degradation was substantially influenced by $^1O_2$ inhibition, as the addition of NaN_3 from 10 to 100 μM suppressed the SMX degradation efficiency from 86 % to 27 % along with a decline in reaction rate constant from 0.037 to 0.007 min^{-1} (Fig. S 8d). The dramatic influence of NaN_3 on SMX degradation could be due to the shorter lifetime of $SO_4^{\bullet-}$ and $^{\bullet}OH$, leading to their transformation to $^1O_2$ [54]. The EPR and quenching results indicate the decisive role of free radicals during the oxidation reaction and provide conclusive evidence for the possible conversion of free radicals to singlet oxygen and its leading role in the catalytic oxidation mechanism.

It was interesting to observe that $^{\bullet}OH$ might be a leading reactive specie that was initially generated during PMS activation, as confirmed by the EPR peak intensities and quenching results. At first, PMS adsorbs onto the $CuFe_2O_4/Fe_2O_3$ catalyst and starts interacting with its hydroxylated surface to form successful PMS* complexes. Afterwards, the surface Fe(III) and Cu(II) species are responsible for PMS* activation via a single electron transfer redox mechanism, forming the $^{\bullet}OH$ radicals (Eq. (3)–(6)) [55]. Moreover, peroxide can also be formed due to the reported hydrolysis equilibrium of HSO_5^- species, resulting in the generation of additional $^{\bullet}OH$ (Eq. (7) [53]. The generated $^{\bullet}OH$ radicals may lead to form $SO_4^{\bullet-}$ radicals, following an indirect generation of $SO_5^{\bullet-}$ (Eq. (8) & (9)). Furthermore, $^1O_2$ can also be produced either by (i) self-decomposition of PMS (Eq. (10), (ii) reaction between $^{\bullet}OH$ and $O_2^{\bullet-}$ (Eq. (11) & (12)) [56], and (iii) reaction between lattice oxygen and added PMS (Eq. (13) [57]. Apparently, $O_2^{\bullet-}$ can be formed by the reaction between produced peroxide and hydroxyl radicals as represented in Eq. (14) & (15). The overall catalytic oxidation of the SMX $CuFe_2O_4/Fe_2O_3$/PMS catalyst system can be presented in a single equation as Eq 0.16, where both radical and non-radical pathways are held accountable for the successful activation of PMS. Moreover, A graphical overview of the process is also depicted in Fig. 10.

$$\equiv Fe\,(III) + HSO_5^- \rightarrow\ \equiv Fe\,(II) + SO_5^{\bullet-} + H^+ \tag{3}$$

$$\equiv Cu\,(II) + HSO_5^- \rightarrow\ \equiv Cu\,(I) + SO_5^{\bullet-} + H^+ \tag{4}$$

$$\equiv Fe\,(II) + HSO_5^- \rightarrow\ \equiv Fe\,(III) + SO_4^{2-} + {}^{\bullet}OH \tag{5}$$

$$\equiv Cu\,(I) + HSO_5^- \rightarrow\ \equiv Cu\,(II) + SO_4^{2-} + {}^{\bullet}OH \tag{6}$$

$$HSO_5^- + H_2O \rightarrow HSO_4^- + H_2O_2 \tag{7}$$

$${}^{\bullet}OH + HSO_5^- \rightarrow SO_5^{\bullet-} + H_2O \tag{8}$$

$$2SO_5^{\bullet-} \rightarrow 2SO_4^{\bullet-} + O_2 \tag{9}$$

$$HSO_5^- + SO_5^{2-} \rightarrow HSO_4^- + SO_4^{2-} + {}^1O_2 \tag{10}$$

$$2O_2^{\bullet-} + 2H^+ \rightarrow H_2O_2 + {}^1O_2 \tag{11}$$

$$O_2^{\bullet-} + 2H^+ \rightarrow H_2O_2 + {}^1O_2 \tag{12}$$

$$O_{lattice} + HSO_5^- \rightarrow HSO_4^- + {}^1O_2 \tag{13}$$

$${}^{\bullet}OH + H_2O_2 \rightarrow HO_2^{\bullet} + H_2O \tag{14}$$

$$HO_2^{\bullet} \rightarrow H^+ + O_2^{\bullet-} \tag{15}$$

$${}^1O_2/{}^{\bullet}OH/SO_4^{\bullet-} + SMX \rightarrow \{\ldots\ Multiple\ Steps\ldots\} \rightarrow CO_2 + H_2O + by\text{-}products \tag{16}$$
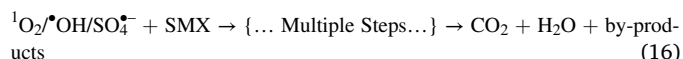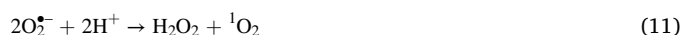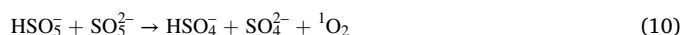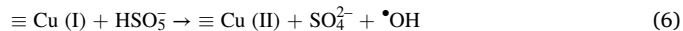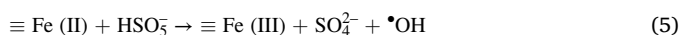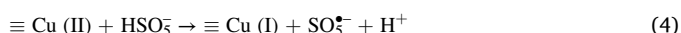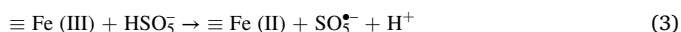
3.6. Mineralisation ability and identification of reaction intermediates

To further evaluate the mineralisation ability of the proposed catalytic system, TOC analyses were performed and are presented in Fig. 11a. In comparison to the respective TOC removal efficiency of 13 % and 29 % by pristine Fe_2O_3/PMS and $CuFe_2O_4$/PMS catalytic system, the CF-0.5/PMS catalytic system depicted a high TOC removal rate of ~ 73 % in just 45 min. This high efficiency indicates the better ability of the employed catalytic system to mineralise the highly stable organic pollutants into less harmful mineral acids and by-products.

To have a more detailed insight into the mineralisation ability, and to interpret the possible degradation mechanism of SMX, UHPLC chromatograms were acquired and thoroughly analysed (Fig. 11b). SMX, at first, was identified by its well-defined peak at retention time (t_R) of 1.43 min. After the addition of PMS, four new peaks emerged at t_R of 0.85, 1.17, 1.94, and 2.90 min. These newly emerged peaks are assigned to the intermediates I_1, I_2, I_3, and I_4. However, previous studies reported multiple reaction intermediates during the degradation experiment, but the presence of only four intermediate peaks in the UHPLC spectra can be ascribed to the very short lifetime and the possible interconversion of those products into a relatively stable intermediate [58–60]. Having an
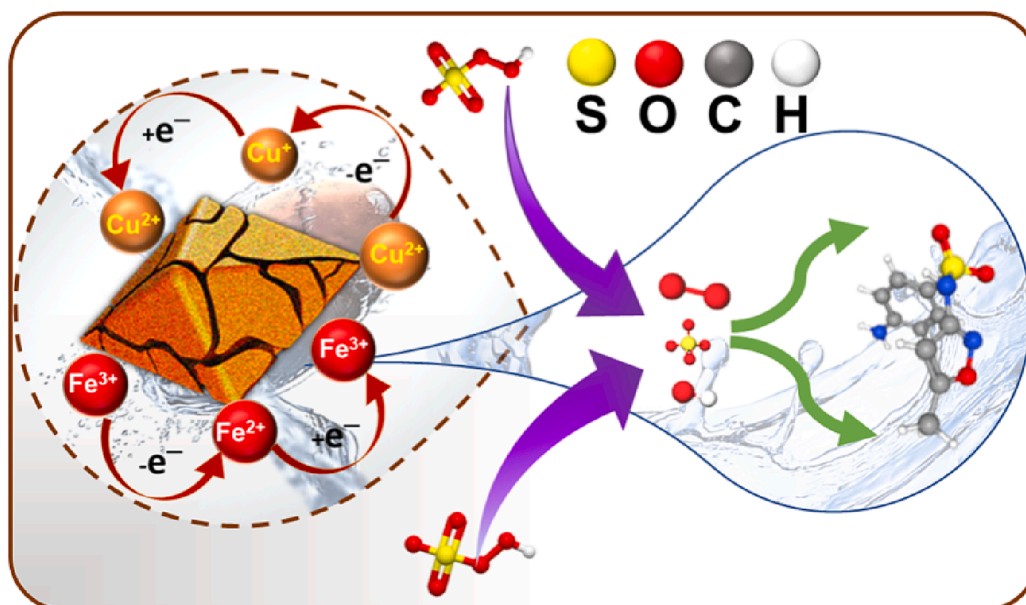
Fig. 10. Proposed SMX degradation mechanism by CF-0.5/PMS catalytic system.
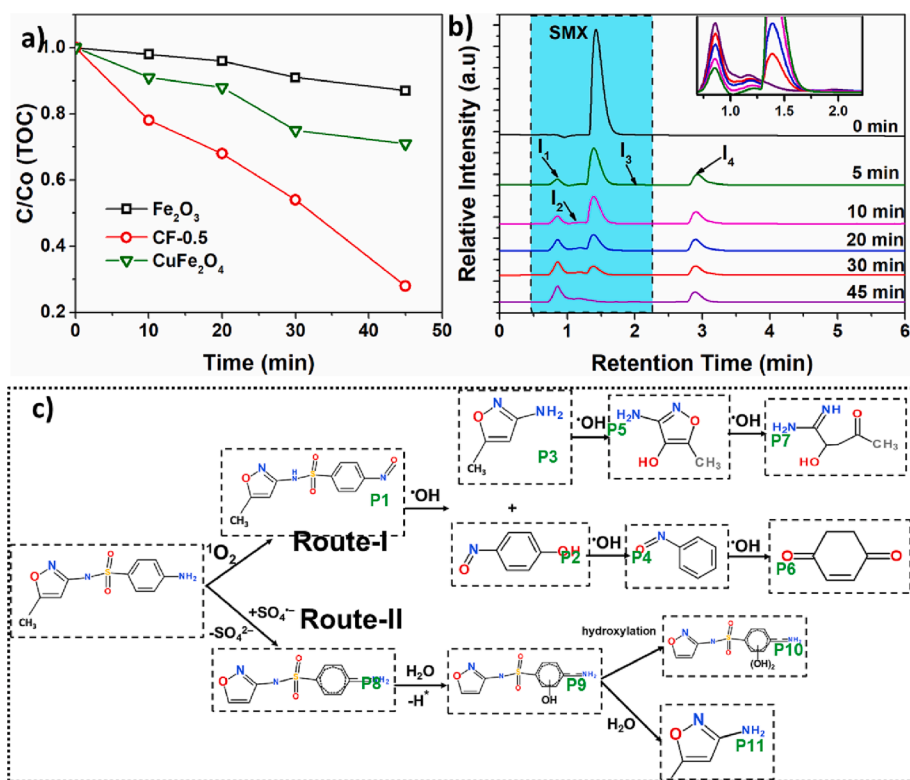
Fig. 11. (a) TOC analyses, (b) HPLC chromatogram, and (c) possible pathways for the degradation of SMX by CF-0.5/PMS system. Reaction Condition: $[Catalyst]_0 = 0.2$ g L^{-1}, $[SMX]_0 = 20$ mg L^{-1}, $[PMS]_0 = 6$ mM, and T $= 25$ °C.

extensive literature review about the intermediates and keeping in view the presence of both radical ($^\bullet$OH, $SO_4^{\bullet-}$, $O^{\bullet-}$), and non-radical ($^1O_2$) species, two possible pathways are proposed for the mineralisation of SMX (Fig. 11c). In Route 1, continuous oxidation of SMX by $^1O_2$ could yield nitroso-SMX (P1), which would be immediately oxidised to products P2 and P3 due to the striking of free radical species [61]. Owing to the hydroxylation and S-N bond cleavage, further oxidation of P2, and P3 by ROS could yield products P4 and P4. Afterwards, the oxidation of P4 may yield p-Benzoquinone (p-BQ), which will ultimately go for ring-opening forming less harmful mineral acids, CO_2, and H_2O [38]. In Route 2, $SO_4^{\bullet-}$ could directly attack the aromatic ring at aniline moiety, yielding a radical cation SMX* (P8), a highly unstable specie and would immediately be converted to SMX-OH (P9) by hydrolysis [62]. Due to the hydroxylation of the benzene ring, P9 could split into two fragments P10, and P11 [60]. Afterwards, the continuous attack of ROS will ultimately lead to the fragmentation towards ring-opening, and mineralisation [63].

4. Conclusion

In summary, MIL-53(Fe) derived $CuFe_2O_4/Fe_2O_3$ perforated microstructures are successfully fabricated via a post solvothermal approach: fragmentally destroying the MIL-53(Fe) structure during a high-temperature in-situ ion-exchange process. All the Cu-modified Fe_2O_3 microstructures are analysed through various physiochemical techniques and are employed for the catalytic oxidation of SMX via PMS activation. Among all CF-x composites, the CF-0.5 shows outstanding catalytic activity towards PMS activation and 99.9 % SMX removal was observed in just 45 min. This excellent performance is attributed to the better textural, morphological, and fine elemental dispersion onto the catalyst surface. Reaction parameters including pH, PMS loading, catalyst dosage, and reaction temperature were further optimised for making it a potential catalytic system for large-scale operations. Moreover, magnetic recovery and high stability are additional benefits associated

with the CF-0.5 catalyst. Quenching experiments and EPR analyses further identify the presence of both radical ($SO_4^{\bullet-}$, $^\bullet$OH, and $O_2^{\bullet-}$) and non-radical ($^1O_2$) species during the degradation process. At last, mineralisation ability was analysed through TOC analyses and possible routes for the mineralisation of SMX are proposed. This study not only provides new insight into the fabrication of MOF-sacrificed structures but also presents the $CuFe_2O_4/Fe_2O_3$ composite as an advantageous catalytic material for the removal of emerging contaminants such as SMX.

CRediT authorship contribution statement

Abdul Hannan Asif: Conceptualization, Methodology, Investigation, Writing – original draft. **Nasir Rafique:** Formal analysis. **Rajan Arjan Kalyan Hirani:** Data curation, Formal analysis. **Lei Shi:** Supervision, Resources. **Yantao Wang:** Formal analysis. **Xiaoguang Duan:** Supervision. **Yu Yin:** Supervision. **Hongqi Sun:** Supervision, Project administration, Writing – review & editing.

Declaration of Competing Interest

The authors declare that they have no known competing financial interests or personal relationships that could have appeared to influence the work reported in this paper.

Data availability

Data will be made available on request.

Acknowledgement

their acknowledgement to Dr. Faisal Awan and Dr. Veena Bobade from School of Engineering, Edith Cowna University for providing their technical support and expertise. The authors are also thankful to the Centre for Microscopy, Characterisation & Analysis (CMCA), The University of Western Australia for providing the technical support for microscopic analysis.

Appendix A. Supplementary material

Supplementary data to this article can be found online at https://doi.org/10.1016/j.cej.2023.143915.

References

[1] S. Hena, L. Gutierrez, J.-P. Croué, Removal of pharmaceutical and personal care products (PPCPs) from wastewater using microalgae: A review, J. Hazard. Mater. 403 (2021) 124041, https://doi.org/10.1016/j.jhazmat.2020.124041.

[2] A.H. Asif, S. Wang, H. Sun, Hematite-based nanomaterials for photocatalytic degradation of pharmaceuticals and personal care products (PPCPs): A short review, Curr. Opin. Green Sustainable Chem. 28 (2021), 100447, https://doi.org/10.1016/j.cogsc.2021.100447.

[3] J. Yan, J. Li, J. Peng, H. Zhang, Y. Zhang, B. Lai, Efficient degradation of sulfamethoxazole by the CuO@Al$_2$O$_3$ (EPC) coupled PMS system: Optimization, degradation pathways and toxicity evaluation, Chem. Eng. J. 359 (2019) 1097–1110, https://doi.org/10.1016/j.cej.2018.11.074.

[4] Q.-Q. Zhang, G.-G. Ying, C.-G. Pan, Y.-S. Liu, J.-L. Zhao, Comprehensive evaluation of antibiotics emission and fate in the River Basins of China: Source analysis, multimedia modeling, and linkage to bacterial resistance, Environ. Sci. Technol. 49 (2015) 6772–6782, https://doi.org/10.1021/acs.est.5b00729.

[5] S.I. Mulla, A. Hu, Q. Sun, J. Li, F. Suanon, M. Ashfaq, C.-P. Yu, Biodegradation of sulfamethoxazole in bacteria from three different origins, J. Environ. Manage. 206 (2018) 93–102, https://doi.org/10.1016/j.jenvman.2017.10.029.

[6] J. Lee, U. von Gunten, J.-H. Kim, Persulfate-based advanced oxidation: Critical assessment of opportunities and roadblocks, Environ. Sci. Technol. 54 (2020) 3064–3081, https://doi.org/10.1021/acs.est.9b07082.

[7] J. Wang, S. Wang, Reactive species in advanced oxidation processes: Formation, identification and reaction mechanism, Chem. Eng. J. 401 (2020) 126158, https://doi.org/10.1016/j.cej.2020.126158.

[8] L. Qin, W. Chen, Y. Fu, J. Tang, H. Yi, L. Li, F. Xu, M. Zhang, W. Cao, D. Huang, C. Lai, Hemin derived iron and nitrogen-doped carbon as a novel heterogeneous electro-Fenton catalyst to efficiently degrade ciprofloxacin, Chem. Eng. J. 449 (2022), 137840, https://doi.org/10.1016/j.cej.2022.137840.

[9] L. Qin, H. Ye, C. Lai, S. Liu, X. Zhou, F. Qin, D. Ma, B. Long, Y. Sun, L. Tang, M. Yan, W. Chen, W. Chen, L. Xiang, Citrate-regulated synthesis of hydrotalcite-like compounds as peroxymonosulfate activator - Investigation of oxygen vacancies and degradation pathways by combining DFT, Appl. Catal. B: Environ. 317 (2022), 121704, https://doi.org/10.1016/j.apcatb.2022.121704.

[10] J. Hou, X. He, S. Zhang, J. Yu, M. Feng, X. Li, Recent advances in cobalt-activated sulfate radical-based advanced oxidation processes for water remediation: A review, Sci. Total Environ. 770 (2021), 145311, https://doi.org/10.1016/j.scitotenv.2021.145311.

[11] J. Cao, L. Lai, B. Lai, G. Yao, X. Chen, L. Song, Degradation of tetracycline by peroxymonosulfate activated with zero-valent iron: Performance, intermediates, toxicity and mechanism, Chem. Eng. J. 364 (2019) 45–56, https://doi.org/10.1016/j.cej.2019.01.113.

[12] M. Kohantorabi, G. Moussavi, S. Giannakis, A review of the innovations in metal- and carbon-based catalysts explored for heterogeneous peroxymonosulfate (PMS) activation, with focus on radical vs. non-radical degradation pathways of organic contaminants, Chem. Eng. J. 411 (2021), 127957, https://doi.org/10.1016/j.cej.2020.127957.

[13] S. Liu, Z. Zhang, F. Huang, Y. Liu, L. Feng, J. Jiang, L. Zhang, F. Qi, C. Liu, Carbonized polyaniline activated peroxymonosulfate (PMS) for phenol degradation: Role of PMS adsorption and singlet oxygen generation, Appl. Catal. B: Environ. 286 (2021), 119921, https://doi.org/10.1016/j.apcatb.2021.119921.

[14] L. Yang, Y. Jiao, X. Xu, Y. Pan, C. Su, X. Duan, H. Sun, S. Liu, S. Wang, Z. Shao, Superstructures with atomic-level arranged perovskite and oxide layers for advanced oxidation with an enhanced non-free radical pathway, ACS Sustainable Chem. Eng. 10 (2022) 1899–1909, https://doi.org/10.1021/acssuschemeng.1c07605.

[15] Q. Qin, T. Liu, J. Zhang, R. Wei, S. You, Y. Xu, Facile synthesis of oxygen vacancies enriched α-Fe$_2$O$_3$ for peroxymonosulfate activation: A non-radical process for sulfamethoxazole degradation, J. Hazard. Mater. 419 (2021), 126447, https://doi.org/10.1016/j.jhazmat.2021.126447.

[16] T. Guo, L. Jiang, K. Wang, Y. Li, H. Huang, X. Wu, G. Zhang, Efficient persulfate activation by hematite nanocrystals for degradation of organic pollutants under visible light irradiation: Facet-dependent catalytic performance and degradation mechanism, Appl. Catal. B: Environ. 286 (2021), 119883, https://doi.org/10.1016/j.apcatb.2021.119883.

[17] Q. Tao, J. Bi, X. Huang, R. Wei, T. Wang, Y. Zhou, H. Hao, Fabrication, application, optimization and working mechanism of Fe$_2$O$_3$ and its composites for contaminants elimination from wastewater, Chemosphere 263 (2021), 127889, https://doi.org/10.1016/j.chemosphere.2020.127889.

[18] S. Xiao, M. Cheng, H. Zhong, Z. Liu, Y. Liu, X. Yang, Q. Liang, Iron-mediated activation of persulfate and peroxymonosulfate in both homogeneous and heterogeneous ways: A review, Chem. Eng. J. 384 (2020), 123265, https://doi.org/10.1016/j.cej.2019.123265.

[19] Y. Peng, H. Tang, B. Yao, X. Gao, X. Yang, Y. Zhou, Activation of peroxymonosulfate (PMS) by spinel ferrite and their composites in degradation of organic pollutants: A review, Chem. Eng. J. 414 (2021), 128800, https://doi.org/10.1016/j.cej.2021.128800.

[20] H. Qin, Y. He, P. Xu, D. Huang, Z. Wang, H. Wang, Z. Wang, Y. Zhao, Q. Tian, C. Wang, Spinel ferrites (MFe$_2$O$_4$): Synthesis, improvement and catalytic application in environment and energy field, Adv. Colloid Interface Sci. 294 (2021), 102486, https://doi.org/10.1016/j.cis.2021.102486.

[21] K.K. Kefeni, B.B. Mamba, T.A.M. Msagati, Application of spinel ferrite nanoparticles in water and wastewater treatment: A review, Sep. Purif. Technol. 188 (2017) 399–422, https://doi.org/10.1016/j.seppur.2017.07.015.

[22] S.-F. Jiang, L.L. Wang, W.-F. Hu, K. Tian, H. Jiang, Preparation of flower-like CuFe$_2$O$_4$ by a self-templating method for high-efficient activation of peroxymonosulfate to degrade carbamazepine, Ind. Eng. Chem. Res. 60 (2021) 11045–11055, https://doi.org/10.1021/acs.iecr.1c02254.

[23] Q. Sun, X. Wang, Y. Liu, S. Xia, J. Zhao, Activation of peroxymonosulfate by a floating oxygen vacancies - CuFe$_2$O$_4$ photocatalyst under visible light for efficient degradation of sulfamethazine, Sci. Total Environ. 824 (2022), 153630, https://doi.org/10.1016/j.scitotenv.2022.153630.

[24] Y. Zhao, D. Lu, C. Xu, J. Zhong, M. Chen, S. Xu, Y. Cao, Q. Zhao, M. Yang, J. Ma, Synergistic oxidation - filtration process analysis of catalytic CuFe$_2$O$_4$ - Tailored ceramic membrane filtration via peroxymonosulfate activation for humic acid treatment, Water Res. 171 (2020), 115387, https://doi.org/10.1016/j.watres.2019.115387.

[25] Y. Cao, Y. Fang, X. Lei, B. Tan, X. Hu, B. Liu, Q. Chen, Fabrication of novel CuFe$_2$O$_4$/MXene hierarchical heterostructures for enhanced photocatalytic degradation of sulfonamides under visible light, J. Hazard. Mater. 387 (2020), 122021, https://doi.org/10.1016/j.jhazmat.2020.122021.

[26] X. Dong, B. Ren, Z. Sun, C. Li, X. Zhang, M. Kong, S. Zheng, D.D. Dionysiou, Monodispersed CuFe$_2$O$_4$ nanoparticles anchored on natural kaolinite as highly efficient peroxymonosulfate catalyst for bisphenol A degradation, Appl. Catal. B: Environ. 253 (2019) 206–217, https://doi.org/10.1016/j.apcatb.2019.04.052.

[27] R.R. Salunkhe, Y.V. Kaneti, Y. Yamauchi, Metal-organic framework-derived nanoporous metal oxides toward supercapacitor applications: progress and prospects, ACS Nano 11 (2017) 5293–5308, https://doi.org/10.1021/acsnano.7b02796.

[28] Y. Li, Y. Xu, W. Yang, W. Shen, H. Xue, H. Pang, MOF-derived metal oxide composites for advanced electrochemical energy storage, Small 14 (2018) 1704435, https://doi.org/10.1002/smll.201704435.

[29] S. Dang, Q.-L. Zhu, Q. Xu, Nanomaterials derived from metal–organic frameworks, Nat. Rev. Mater. 3 (2017) 17075, https://doi.org/10.1038/natrevmats.2017.75.

[30] Z. Xiong, Y. Jiang, Z. Wu, G. Yao, B. Lai, Synthesis strategies and emerging mechanisms of metal-organic frameworks for sulfate radical-based advanced oxidation process: A review, Chem. Eng. J. 421 (2021), 127863, https://doi.org/10.1016/j.cej.2020.127863.

[31] P. Man, Q. Zhang, Z. Zhou, M. Chen, J. Yang, Z. Wang, Z. Wang, B. He, Q. Li, W. Gong, W. Lu, Y. Yao, L. Wei, Engineering MoS$_2$ nanosheets on spindle-like α-Fe$_2$O$_3$ as high-performance core-shell pseudocapacitive anodes for fiber-shaped aqueous lithium-ion capacitors, Adv. Funct. Mater. 30 (2020) 2003967, https://doi.org/10.1002/adfm.202003967.

[32] J. Yan, J. Peng, L. Lai, F. Ji, Y. Zhang, B. Lai, Q. Chen, G. Yao, X. Chen, L. Song, Activation CuFe$_2$O$_4$ by hydroxylamine for oxidation of antibiotic sulfamethoxazole, Environ. Sci. Technol. 52 (2018) 14302–14310, https://doi.org/10.1021/acs.est.8b03340.

[33] X. Zhang, B. Lin, X. Li, X. Wang, K. Huang, Z. Chen, MOF-derived magnetically recoverable Z-scheme ZnFe$_2$O$_4$/Fe$_2$O$_3$ perforated nanotube for efficient photocatalytic ciprofloxacin removal, Chem. Eng. J. 430 (2022), 132728, https://doi.org/10.1016/j.cej.2021.132728.

[34] C. Zhang, L. Ai, J. Jiang, Solvothermal synthesis of MIL–53(Fe) hybrid magnetic composites for photoelectrochemical water oxidation and organic pollutant photodegradation under visible light, J. Mater. Chem. A 3 (2015) 3074–3081, https://doi.org/10.1039/C4TA04622F.

[35] Q. Zhang, J.-B. Liu, L. Chen, C.-X. Xiao, P. Chen, S. Shen, J.-K. Guo, C.-T. Au, S.-F. Yin, An etching and re-growth method for the synthesis of bismuth ferrite/MIL-53(Fe) nanocomposite as efficient photocatalyst for selective oxidation of aromatic alcohols, Appl. Catal. B: Environ. 264 (2020), 118529, https://doi.org/10.1016/j.apcatb.2019.118529.

[36] S.M. Rathod, A.R. Chavan, S.S. Jadhav, K.M. Batoo, M. Hadi, E.H. Raslan, Ag$^+$ ion substituted CuFe$_2$O$_4$ nanoparticles: Analysis of structural and magnetic behavior, Chem. Phys. Lett. 765 (2021) 138308, https://doi.org/10.1016/j.cplett.2020.138308.

[37] X. Zhao, Y. Tan, F. Wu, H. Niu, Z. Tang, Y. Cai, J.P. Giesy, Cu/Cu$_2$O/CuO loaded on the carbon layer derived from novel precursors with amazing catalytic performance, Sci. Total Environ. 571 (2016) 380–387, https://doi.org/10.1016/j.scitotenv.2016.05.151.

[38] A.H. Asif, N. Rafique, R.A.K. Hirani, H. Wu, L. Shi, S. Zhang, S. Wang, Y. Yin, M. Saunders, H. Sun, Morphology/facet-dependent photo-Fenton-like degradation of pharmaceuticals and personal care products over hematite nanocrystals, Chem. Eng. J. 432 (2022), 134429, https://doi.org/10.1016/j.cej.2021.134429.

[39] A.H. Asif, N. Rafique, R.A.K. Hirani, L. Shi, S. Zhang, S. Wang, H. Sun, Graphitic carbon nitride engineered α-Fe$_2$O$_3$/rGO heterostructure for visible-light-driven

photochemical oxidation of sulfamethoxazole, Chem. Eng. J. 451 (2023), 138630, https://doi.org/10.1016/j.cej.2022.138630.

[40] K. Cao, L. Jiao, H. Liu, Y. Liu, Y. Wang, Z. Guo, H. Yuan, 3D hierarchical porous α-Fe$_2$O$_3$ nanosheets for high-performance lithium-ion batteries, Adv. Energy Mater. 5 (2015) 1401421, https://doi.org/10.1002/aenm.201401421.

[41] Y. Zhang, C. Liu, B. Xu, F. Qi, W. Chu, Degradation of benzotriazole by a novel Fenton-like reaction with mesoporous Cu/MnO$_2$: Combination of adsorption and catalysis oxidation, Appl. Catal. B: Environ. 199 (2016) 447–457, https://doi.org/10.1016/j.apcatb.2016.06.003.

[42] Z. Li, C. Guo, J. Lyu, Z. Hu, M. Ge, Tetracycline degradation by persulfate activated with magnetic Cu/CuFe$_2$O$_4$ composite: Efficiency, stability, mechanism and degradation pathway, J. Hazard. Mater. 373 (2019) 85–96, https://doi.org/10.1016/j.jhazmat.2019.03.075.

[43] J. Liu, Z. Jia, W. Zhou, X. Liu, C. Zhang, B. Xu, G. Wu, Self-assembled MoS$_2$/magnetic ferrite CuFe$_2$O$_4$ nanocomposite for high-efficiency microwave absorption, Chem. Eng. J. 429 (2022), 132253, https://doi.org/10.1016/j.cej.2021.132253.

[44] Y. Sun, H. Xie, C. Zhou, Y. Wu, M. Pu, J. Niu, The role of carbonate in sulfamethoxazole degradation by peroxymonosulfate without catalyst and the generation of carbonate racial, J. Hazard. Mater. 398 (2020), 122827, https://doi.org/10.1016/j.jhazmat.2020.122827.

[45] R. Yin, W. Guo, H. Wang, J. Du, X. Zhou, Q. Wu, H. Zheng, J. Chang, N. Ren, Selective degradation of sulfonamide antibiotics by peroxymonosulfate alone: Direct oxidation and nonradical mechanisms, Chem. Eng. J. 334 (2018) 2539–2546, https://doi.org/10.1016/j.cej.2017.11.174.

[46] L. Liu, H. Mi, M. Zhang, F. Sun, R. Zhan, H. Zhao, S. He, L. Zhou, Efficient moxifloxacin degradation by CoFe$_2$O$_4$ magnetic nanoparticles activated peroxymonosulfate: Kinetics, pathways and mechanisms, Chem. Eng. J. 407 (2021), 127201, https://doi.org/10.1016/j.cej.2020.127201.

[47] B. Liu, W. Song, H. Wu, Z. Liu, Y. Teng, Y. Sun, Y. Xu, H. Zheng, Degradation of norfloxacin with peroxymonosulfate activated by nanoconfinement Co$_3$O$_4$@CNT nanocomposite, Chem. Eng. J. 398 (2020), 125498, https://doi.org/10.1016/j.cej.2020.125498.

[48] H. Zheng, J. Bao, Y. Huang, L. Xiang, Faheem, B. Ren, J. Du, M.N. Nadagouda, D.D. Dionysiou, Efficient degradation of atrazine with porous sulfurized Fe$_2$O$_3$ as catalyst for peroxymonosulfate activation, Appl. Catal. B: Environ., 259 (2019) 118056 https://doi.org/10.1016/j.apcatb.2019.118056.

[49] S. Guo, H. Wang, W. Yang, H. Fida, L. You, K. Zhou, Scalable synthesis of Ca-doped α-Fe$_2$O$_3$ with abundant oxygen vacancies for enhanced degradation of organic pollutants through peroxymonosulfate activation, Appl. Catal. B: Environ. 262 (2020), 118250, https://doi.org/10.1016/j.apcatb.2019.118250.

[50] W. Qin, G. Fang, Y. Wang, D. Zhou, Mechanistic understanding of polychlorinated biphenyls degradation by peroxymonosulfate activated with CuFe$_2$O$_4$ nanoparticles: Key role of superoxide radicals, Chem. Eng. J. 348 (2018) 526–534, https://doi.org/10.1016/j.cej.2018.04.215.

[51] J. Yang, Z. Li, H. Zhu, Adsorption and photocatalytic degradation of sulfamethoxazole by a novel composite hydrogel with visible light irradiation, Appl. Catal. B: Environ. 217 (2017) 603–614, https://doi.org/10.1016/j.apcatb.2017.06.029.

[52] A.H. Asif, N. Rafique, R.A.K. Hirani, H. Wu, L. Shi, H. Sun, Heterogeneous activation of peroxymonosulfate by Co-doped Fe$_2$O$_3$ nanospheres for degradation of p-hydroxybenzoic acid, J. Colloid Interface Sci. 604 (2021) 390–401, https://doi.org/10.1016/j.jcis.2021.06.161.

[53] Y. Xu, J. Ai, H. Zhang, The mechanism of degradation of bisphenol A using the magnetically separable CuFe$_2$O$_4$/peroxymonosulfate heterogeneous oxidation process, J. Hazard. Mater. 309 (2016) 87–96, https://doi.org/10.1016/j.jhazmat.2016.01.023.

[54] C. Dong, Y. Bao, T. Sheng, Q. Yi, Q. Zhu, B. Shen, M. Xing, I.M.C. Lo, J. Zhang, Singlet oxygen triggered by robust bimetallic MoFe/TiO$_2$ nanospheres of highly efficacy in solar-light-driven peroxymonosulfate activation for organic pollutants removal, Appl. Catal. B: Environ. 286 (2021), 119930, https://doi.org/10.1016/j.apcatb.2021.119930.

[55] B. He, L. Song, Z. Zhao, W. Liu, Y. Zhou, J. Shang, X. Cheng, CuFe$_2$O$_4$/CuO magnetic nano-composite activates PMS to remove ciprofloxacin: Ecotoxicity and DFT calculation, Chem. Eng. J. 446 (2022), 137183, https://doi.org/10.1016/j.cej.2022.137183.

[56] J.-C.-E. Yang, Y. Lin, H.-H. Peng, B. Yuan, D.D. Dionysiou, X.-D. Huang, D.-D. Zhang, M.-L. Fu, Novel magnetic rod-like Mn-Fe oxycarbide toward peroxymonosulfate activation for efficient oxidation of butyl paraben: Radical oxidation versus singlet oxygenation, Appl. Catal. B: Environ. 268 (2020), 118549, https://doi.org/10.1016/j.apcatb.2019.118549.

[57] R.A.K. Hirani, A.H. Asif, N. Rafique, H. Wu, L. Shi, S. Zhang, X. Duan, S. Wang, M. Saunders, H. Sun, Three-dimensional nitrogen-doped graphene oxide beads for catalytic degradation of aqueous pollutants, Chem. Eng. J. 446 (2022), 137042, https://doi.org/10.1016/j.cej.2022.137042.

[58] S. Wang, Y. Liu, J. Wang, Iron and sulfur co-doped graphite carbon nitride (FeO$_y$/S-g-C$_3$N$_4$) for activating peroxymonosulfate to enhance sulfamethoxazole degradation, Chem. Eng. J. 382 (2020), 122836, https://doi.org/10.1016/j.cej.2019.122836.

[59] Z. He, H. Wang, M. Li, L. Feng, J. Niu, Z. Li, X. Jia, G. Hu, Amorphous cobalt oxide decorated halloysite nanotubes for efficient sulfamethoxazole degradation activated by peroxymonosulfate, J. Colloid Interface Sci. 607 (2022) 857–868, https://doi.org/10.1016/j.jcis.2021.08.168.

[60] Y. Yu, Y. Ji, J. Li, X. Yin, Q. Zhou, Degradation of sulfamethoxazole by Co$_3$O$_4$-palygorskite composites activated peroxymonosulfate oxidation, Chem. Eng. J. 406 (2021), 126759, https://doi.org/10.1016/j.cej.2020.126759.

[61] J. Du, W. Guo, H. Wang, R. Yin, H. Zheng, X. Feng, D. Che, N. Ren, Hydroxyl radical dominated degradation of aquatic sulfamethoxazole by Fe^0/bisulfite/O$_2$: Kinetics, mechanisms, and pathways, Water Res. 138 (2018) 323–332, https://doi.org/10.1016/j.watres.2017.12.046.

[62] Y. Ji, Y. Fan, K. Liu, D. Kong, J. Lu, Thermo activated persulfate oxidation of antibiotic sulfamethoxazole and structurally related compounds, Water Res. 87 (2015) 1–9, https://doi.org/10.1016/j.watres.2015.09.005.

[63] P. Yan, Q. Sui, S. Lyu, S. Hao, H.F. Schröder, W. Gebhardt, Elucidation of the oxidation mechanisms and pathways of sulfamethoxazole degradation under Fe(II) activated percarbonate treatment, Sci. Total Environ. 640–641 (2018) 973–980, https://doi.org/10.1016/j.scitotenv.2018.05.315.